Dalton Transactions

ROYAL SOCIETY OF CHEMISTRY

PAPER

View Article Online
View Journal | View Issue

Check for updates

Cite this: *Dalton Trans.*, 2020, **49**, 3830

Functional biohybrid materials based on halloysite, sepiolite and cellulose nanofibers for health applications†

Lorenzo Lisuzzo, [a,b] Bernd Wicklein, [b] Giulia Lo Dico, [a] Giuseppe Lazzara, [a] Gustavo del Real, [c] Pilar Aranda [b] and Eduardo Ruiz-Hitzky *[b]

Received 25th September 2019,
Accepted 28th November 2019

DOI: 10.1039/c9dt03804c

rsc.li/dalton

Biohybrid materials were prepared by co-assembling the three following components: nanotubular halloysite, microfibrous sepiolite, and cellulose nanofibers dispersed in water, in order to exploit the most salient features of each individual component and to render homogeneous, flexible, yet strong films. Indeed, the incorporation of halloysite improves the mechanical performance of the resulting hybrid nanopapers and the assembly of the three components modifies the surface features concerning wetting properties compared to pristine materials, so that the main characteristics of the resulting materials become tunable with regard to certain properties. Owing to their hierarchical porosity together with their diverse surface characteristics, these hybrids can be used in diverse biomedical/pharmaceutical applications. Herein, for instance, loading with two model drugs, salicylic acid and ibuprofen, allows controlled and sustained release as deduced from antimicrobial assays, opening a versatile path for developing other related organic–inorganic materials of potential interest in diverse application fields.

1. Introduction

Biohybrid materials attract the interest of both scientific and engineering communities due to their extensive use in a wide range of application fields from environmental remediation to biomedical uses and represent an alternative approach to conventional technologies for combining organic and inorganic moieties by adding particles for which at least one dimension is in the nanometer range.[1–6] Of particular relevance are those systems in which the inorganic component is a silicate belonging to the family of clay minerals, giving rise to nanocomposite materials involving porous and layered silicates.[7–12] The resulting materials may exhibit markedly improved mechanical, thermal, optical, and physicochemical properties compared to those of the pure polymer or conventional (microscale) composites,[13] as first demonstrated by Fukushima and co-workers for nylon–clay nanocomposites.[14] In recent years, nanocellulose based materials have been the focus of active research with the aim of developing a wide variety of hybrid materials for applications in adaptive and responsive materials, energy storage and conversion, water treatment, biomedicine, packaging, fire retardancy, as a support for metal and metal oxide nanoparticles in catalysts, and electronics.[15–20] In this context, the concept of "nanopaper" refers to the use of cellulose nanofibers (CNFs) for making paper instead of employing conventional, micronized cellulose pulp. The term "nanocellulose" refers to a family of cellulose nanomaterials (fibers and crystals) obtained from different chemical and mechanical methodologies that provoke a defibrillation process in raw cellulosic materials.[21,22] Cellulose nanofibers show a high aspect ratio (up to 1 μm in length and 2–5 nm in thickness), a chemically modifiable surface, and a high elastic modulus resulting from their high crystallinity,[23] and are prepared by relatively low-expensive production methods, all of which endow CNFs with great potential for the fabrication of numerous functional structures.[24,25] Recent studies on CNFs have been dealing with their assembly to other nanobuilding blocks of an inorganic nature, for instance, the combination of CNFs with layered silicates, such as vermiculite to produce biohybrids used as packaging material,[26] montmorillonite to develop materials showing high mechanical performance,[27] or the preparation of functional, heterofibrous hybrid materials by an integrative approach from the dispersions of nanofibrillated cellulose and defibrillated sepiolite.[28,29] Sepiolite is a microcrystalline

[a]Department of Physics and Chemistry, University of Palermo, Viale delle Scienze, pad. 17, Palermo 90128, Italy
[b]Instituto de Ciencia de Materiales de Madrid (ICMM), Consejo Superior de Investigaciones Científicas (CSIC), c/Sor Juana Inés de la Cruz 3, 28049 Madrid, Spain. E-mail: eduardo@icmm.csic.es
[c]Instituto Nacional de Investigación y Tecnología Agraria y Alimentaria (INIA), Ctra. de la Coruña km 7.5, 28040 Madrid, Spain

†Electronic supplementary information (ESI) available. See DOI: 10.1039/C9DT03804C

hydrated magnesium silicate with $Si_{12}O_{30}Mg_8(OH,F)_4(H_2O)_4 \cdot 8H_2O$ as the theoretical unit cell formula.[30] Indeed, sepiolite shows a microfibrous morphology with a particle size typically in the 0.5–2 μm length range.[31] Structurally, it is formed by the alternation of blocks and cavities (tunnels) that grow in the fiber direction (*c*-axis). Each structural block is composed of two tetrahedral silica sheets sandwiching a central sheet of magnesium oxide-hydroxide. Owing to the discontinuity of the silica sheets, the channels and silanol groups (Si–OH) are present on the external surface of the silicate particles.[32] These groups are located at the edges of the channels (*i.e.* those tunnels acceding to the external surface of the silicate) and are directly accessible to different species, thus representing the only sites available for functionalization. Moreover, one of the most interesting features of sepiolite is its very high colloidal stability in aqueous media that has been exploited for stabilizing, among others, carbon nanotubes and graphene nanoplatelet suspensions.[33,34] In light of these properties and features, it is clear that sepiolite represents a very interesting starting building block for designing a wide class of smart materials.[35] Nevertheless, one limitation of sepiolite is its restriction only to its external surface during the interaction with other active and bulky species due to the reduced accessibility of the Mg–OH groups located inside the microporous tunnels.[30]

Hence, the use of further components to overcome this limitation and to fully exploit the features of sepiolite and to develop potential synergistic effects is pursued here through the co-assembly of clay nanotubes.

Halloysite (HNT) is structurally a 1 : 1 layered alumino-silicate clay showing a tubular morphology with an external diameter of 50–80 nm, an internal diameter of 10–15 nm, and a length of *ca.* 1000 nm.[36–38] Interestingly, it displays a positively charged lumen and a negatively charged outer surface in the pH range between 2 and 8.[39,40] This characteristic is due to the different chemical compositions: the external surface is composed of Si–O–Si groups while the inner surface consists of a gibbsite-like array of Al–OH groups.[41] This peculiar surface chemistry makes possible, in contrast to sepiolite, a selective targeted modification driven by electrostatic interactions.[42–44] These groups allow the clay to participate in electrostatic or hydrogen bonding in polar solvents and to interact favorably with the functional groups of a wide range of chemical species.[45–48] Due to various characteristics such as a nanoscale lumen, high aspect ratio, relatively low hydroxyl group density on the surface, *etc*., numerous advanced applications have been discovered for this unique, cheap, and abundant clay.[49–55] Moreover, HNTs are biocompatible as shown in several *in vitro* and *in vivo* studies.[56] Beyond these aspects, one of the limitations to the use of pristine halloysite is its low colloidal stability in aqueous suspensions, which hampers its use and applicability except for adequately modified HNTs.[57] In this way, we have recently reported a protocol to produce multicomponent conductive bionanocomposite materials where the use of sepiolite is fundamental to achieve the stabilization of HNT dispersions in which the other components can be homogeneously incorporated.[58]

In this context, the main objective of this work is to develop an alternative strategy for the preparation of a new type of multicomponent hybrid nanopaper constituted by cellulose nanofibers, sepiolite, and halloysite. Our purpose is to investigate the possibility to exploit the most important features of each component and to overcome their individual limitations in order to design a material with different chemical surfaces. Here, a hybrid material was prepared for drug delivery applications exemplified by using two cationic model drugs. Ibuprofen is a hydrophobic,[59] non-steroidal, anti-inflammatory drug (NSAID) that is administered for the relief of moderate pain and inflammation.[60] On the other hand, salicylic acid was tested for its bactericidal and antiseptic properties, and is used in a wide range of pharmaceutical formulations and as an additive for food and cosmetics.[61] In light of the above, the possibilities of developing a multicomponent hybrid nanopaper possessing different types of chemical surfaces that can selectively interact with active species and can sustain, control and optimize their release on time represent a crucial point.

2. Experimental details

2.1. Materials

Sepiolite was obtained from Vicálvaro-Vallecas deposits, Madrid (Spain), with >95% purity. Commercialized as Pangel S9, sepiolite of rheological grade was supplied by Tolsa S.A. (Spain) and was used as supplied. Halloysite (New Zealand China Clays) was supplied by Imerys (France). Ibuprofen sodium salt (IBU) and sodium salicylate (SS) were purchased from Sigma Aldrich. The solubility of IBU (100 mg ml^{-1}) and SA (100 mg ml^{-1}) in water was tested according to Sigma Aldrich specification sheets. Deionized water (18.2 MΩ cm) was obtained using a Maxima Ultra Pure Water system from Elga. Sodium phosphate tribasic dodecahydrate (≥98%) and sodium hydroxide (≥98%) were supplied by Sigma Aldrich and phosphoric acid (85%) by Carlo Erba.

The preparation of CNFs used in this work was carried out through the TEMPO-mediated oxidation of eucalyptus pulp following the procedure described by Fillat *et al.*[62] The resulting cellulose nanofibers were stored at 4 °C.

2.2. Halloysite nanotube drug loading

The loading of IBU and SA into the HNT lumen was achieved by following the procedure described elsewhere for similar systems.[63] Pristine HNTs were added to a saturated aqueous solution of the drugs and then magnetically stirred for *ca.* 1 h. In particular, to prepare the SA loaded HNTs, 1 g of halloysite powder was added to a concentrated solution of sodium–SA in water. The pH was adjusted to 8 by adding 0.1 M NaOH in order to optimize the loading efficiency of SA through maximizing the negative charge of salicylate. Ibuprofen was loaded into halloysite powder from a saturated solution of IBU sodium salt at a 2 : 1 wt ratio. The obtained dispersions were

transferred to a vacuum vessel and evacuated with a vacuum pump (P-Selecta Vacuo-TEM). The HNT–IBU suspensions were subjected to three vacuum cycles to ensure the infiltration of the HNT lumen.[64] The HNT–SA suspension, instead, was kept under vacuum for 3 hours, and the step was repeated three times.

Afterwards, the loaded HNTs were separated from the solution by centrifugation, washed with water and dried overnight.

2.3. Preparation of HNT–SEP–CNF hybrid nanopapers

The ratio (w/w) of HNT, SEP, and CNF was fixed at 1 : 1 : 1 even though many compositions were tested. Typically, SEP (10 mg) was dispersed in 20 mL of water and mixed with 1 g of a CNF gel prepared at 1 wt% in water using an Ultra-Turrax (IKA® T25) homogenizer. Then, 10 mg of pristine HNT were added and the HNT-SEP-CNF mixture was tip-sonicated (Vibra Cell VC 750, 13 mm titanium sonication probe) until a total energy of 1 kJ or 5 kJ was achieved. The films were prepared by casting the mixture in polystyrene Petri dishes followed by drying in a Climacell EVO 111 L climate chamber for 72 h at 30 °C and 60% relative humidity (RH) to obtain hybrid nanopapers with a thickness around 20 μm. The samples were labeled as HNT–SEP–CNF.

HNT–SEP (1 : 1 w/w), HNT–CNF (1 : 1 w/w), SEP–CNF (1 : 1 w/w) and pure CNF films were also prepared by following the same procedure.

2.4. Preparation of drug loaded HNT–SEP–CNF hybrid nanopapers

When drug loaded HNTs were used instead of neat HNTs, halloysite was added after the sonication process to prevent any degradation of drug molecules that could be produced because of the high energy applied to the system. Moreover, to achieve a higher HNT dispersion, the system was sonicated using a simple ultrasound bath (J.P. Selecta) for a few minutes. The same solvent casting procedure was followed.

2.5. Characterization

SEM analysis was performed on Cr metallized samples by using a Philips XL 30 S-FEG field emission scanning electron microscope (FE-SEM). Nanopaper cross-sections were obtained by cutting the films after immersion in liquid N_2. An energy-dispersive X-ray (EDX) spectroscope coupled to an (FEI NOVA Nano SEM 230) FE-SEM was used for elemental mapping. The EDX maps were recorded with a Type SDD Apollo 10 EDAX detector and the data acquisition conditions were kept constant at a working distance of 6.5 mm with a spot size of 50 μm and an energy of 12 kV, for 4200 counts. Atomic force microscopy (AFM) was performed in dynamic mode and under environmental conditions, and this operation provides topographical images of the surface. A Cervantes instrument from Nanotec Electrónica S.L. equipped with a PPP-FMR (a strength constant of 1.5 N m^{-1}) and with a resonance constant of 70 kHz was used. The XRD patterns of HNT and SEP powder and the CNF and HNT–SEP–CNF nanopapers were obtained using a BRUKER D8-ADVANCE diffractometer with copper Kα radiation. The voltage and current sources were set at 40 kV and 30 mA, respectively. Diffraction patterns were recorded with a goniometer speed of 0.5 s per step between 4° and 70° (2θ). FTIR spectra were obtained using a Bruker iFS 66VS spectrophotometer with 2 cm^{-1} resolution. The Young's modulus of the hybrid nanopapers was measured with a DMA Q800 apparatus (TA Instruments). The test specimen was cut in a rectangular shape (10 × 6 mm^2) and the tensile tests were carried out with a stress ramp of 1 MPa min^{-1} at 26.0 ± 0.5 °C. At least three measurements were carried out for each material.

Water sorption isotherms were measured with an Aquadyne DVS from Quantachrome Instrument. Mass changes due to water adsorption or desorption were recorded at 25 °C in the range of relative humidity from 0% to 95%. Halloysite and sepiolite were analyzed as powder, whereas CNF and HNT–SEP–CNF hybrid nanopapers were analyzed as films.

Contact angle experiments were performed by using an optical contact angle apparatus (OCA 20, Data Physics Instruments) equipped with a video measuring system having a high-resolution CCD camera and a high-performance digitizing adapter. The SCA 20 software (Data Physics Instruments) was used for data acquisition. The contact angle of water in air was measured by the sessile drop method. The water droplet volume was 10.0 ± 0.5 μL. The temperature was set at 25.0 ± 0.1 °C for the support and the injecting syringe as well. From the data analysis the contact angle and the volume of the drop were calculated.

Chemical analysis (CHN) was performed using an elemental analyzer (PerkinElmer, 2400 Series II).

The study of the specific surface area and the pore size distribution of samples was carried out through recording nitrogen absorption/desorption isotherms with a Micromeritics ASAP 2010 equipment. The samples were degassed at 100 °C prior to the measurements. From the adsorption isotherm, the value of the specific surface was deduced using the BET method. The pore area and volume were analyzed from the adsorption isotherm using the Barret–Joyner–Hallenda (BJH) method.

2.6. Release kinetics

The release kinetics of the drug loaded pristine HNT was investigated in phosphate buffer 0.1 mol L^{-1} at pH = 5 (which better simulates the skin's natural pH value). The suspension of the drug loaded HNT was placed in a shaking incubator (Julabo SW23) at 37 °C and 150 rpm to establish the equilibrium conditions. At certain predetermined time intervals, 2 ml of the solution was taken out from each sample, and 2 ml of fresh PBS was replaced. The samples for analysis were separated by centrifugation to eliminate light scattering from the halloysite. The collected supernatant was analyzed by carrying out UV-vis measurements (Shimadzu UV-1201) at 264 nm for IBU and at 296 nm for SA.

The following formula:[65]

$$C'_n = C_n + \frac{V}{V_0}\sum_{i=0}^{n-1} C_i \quad (1)$$

corrects the concentration of release, where C'_n is the corrected concentration, C_n represents the nth concentration, V is the sample volume (2 mL), and V_0 is the total volume.

The release kinetics of the drug loaded HNT–SEP–CNF hybrid nanopapers was investigated under the same conditions, but a portion of the film was put into phosphate buffer (pH = 5) and the samples for analysis were taken from the solution and then separated by centrifugation and analyzed.

Before recording the release kinetics of SA and IBU from the loaded HNTs and from the HNT–SEP–CNF hybrid nanopapers, two calibration curves of the drugs in phosphate buffer at pH = 5 were determined. Their measured slopes are 21.63 ± 0.07 mL mg^{-1} for SA and 1.482 ± 0.004 mL mg^{-1} for IBU, respectively.

2.7. Antimicrobial activity

The antimicrobial activity of the SA loaded hybrid nanopapers was investigated against Gram-negative bacteria *Escherichia coli* WDCM 00012 and Gram-positive bacteria *Staphylococcus aureus* WDCM 00034 by the disk diffusion method. The strains were cultured in nutrient broth (Merck, Germany) overnight at 37 °C. Each bacterial culture was swabbed uniformly across nutrient agar plates (Merck, Germany) and allowed to be absorbed for 15 min. The discs (6 mm in diameter) of the hybrid nanopapers were placed aseptically on the surface of the agar plate and the plates were placed in a 37 °C incubator for 24 h. The antibacterial activity of the tested samples was determined by measuring the diameter of the inhibition area around the discs. Studies of the SA loaded nanopapers were conducted at pH = 7.0 and pH = 5.5. The discs were loaded with 10 μL of salicylate solutions in water at various concentrations (20 μg μL^{-1}, 2 μg μL^{-1}, 1 μg μL^{-1}, 0.1 μg μL^{-1}, 0.02 μg μL^{-1}, and 0.004 μg μL^{-1}) (Fig. S6†). The negative controls were the HNT–SEP–CNF discs without the drug.

3. Results and discussion

3.1. Preparation and characterization of the hybrid nanopapers

The microscopic features of the fibrous (SEP) and tubular (HNT) nanoclays and the morphology of the resulting hybrid nanopapers were first studied by electron microscopy. Fig. 2a shows that halloysite consists of fine nanotubes with 50–200 nm external diameter. The length of the tubes largely varies between 100 and 3000 nm. It can also be observed that these HNT samples contain some kaolinite particles (arrows in Fig. 2a). It is well known that both alumino-phyllosilicates (HNT and kaolinite) show a similar structural silica/alumina arrangement and composition but different morphological characteristics (tubular *vs.* hexagonal). Moreover, the microfibrous morphology of sepiolite with a fiber length of 0.5–2 μm and a thickness of *ca.* 30–50 nm is shown in Fig. 2b. The typical fibrous morphology of the CNFs was clearly observed by atomic force microscopy (Fig. 2c). The CNFs consist of 2–4 nm thick fibers of 300–600 nm in length and the characteristic semi-flexibility is revealed by the fiber kinks between the crystalline domains (arrows in Fig. 2c).[25]

The microstructure of the HNT–SEP–CNF (1 : 1 : 1 w/w) hybrid nanopaper was examined from the surface and cross sectional images of the films. The FE-SEM images show the presence of all three components though HNTs are more clearly distinguished due to their larger size (Fig. 3a). It is noteworthy that the two fibrous components (sepiolite and CNFs) cannot be easily distinguished at this magnification due to their morphological similarity and the small width of the CNF fibers as already reported by González del Campo *et al.*[28] The homogeneous distribution of all three components in the hybrid nanopaper was confirmed by EDX mapping (Fig. S1†). The surface images reveal a certain nematic arrangement of the nanofibers (Fig. 3a) which is also visible within the film (Fig. 3b). In fact, the fracture surface morphology of the film resembles the stratified layer structure typical of solvent cast assemblies of nanofibers or nanosheets.[66] These observations are also in agreement with the recently reported tendency of the CNFs for nematic ordering during film drying from pure CNF suspensions resulting in a plywood-like nanostructure of the evaporation-condensed films as a result of the averaging of the polydomain nematic arrangement of the CNF layers.[67] It is remarkable that the nematic arrangement also prevails in the multi-component HNT–SEP–CNF hybrid nanopaper and not only in pure CNF films. The CNFs are characterized by a squared cross-section[68] and the presence of carboxylate and hydroxyl groups that can partake in hydrogen bond formation in different directions. In addition, as the density of the carboxylate groups varies between the crystalline and disordered regions along the CNF fiber length,[69] the nanofiber assembly leads to a lower degree of lateral alignment. The non-uniform distribution of the –OH and $–COO^-$ groups along the CNF length, combined with the nanofiber flexibility provided by the disordered regions, allows for hydrogen bond formation not only with the –OH groups on the side facets of other CNFs but, more importantly, also with the Si–OH groups present at the edges of the sepiolite fibers. This explanation is in good agreement with what has already been observed elsewhere on nematic ordering in a multicomponent system composed of CNFs and V_2O_5 nanofibers.[25] Eventually, this behavior can open up possibilities to tailor the texture and microstructure of complex composite materials with implications of their mechanical, optical and transport properties.

We studied the film formation by considering the components in pairs (*cf.* Fig. 4b–d) and also by changing the ratio between all three components in the HNT–SEP–CNF hybrid nanopaper. It was observed that the 1 : 1 : 1 (w/w) ratio gave better results than the other compositions considering the macroscopic aspect, film consistency and homogeneity. This is most likely due to the association between the various building blocks processed as shown in the scheme in Fig. 1. Hence, the multicomponent HNT–SEP–CNF hybrid nanopaper was prepared at a ratio of 1 : 1 : 1 (w/w), which displayed the best film forming behaviour (Fig. 4a). Interestingly, not only the compo-

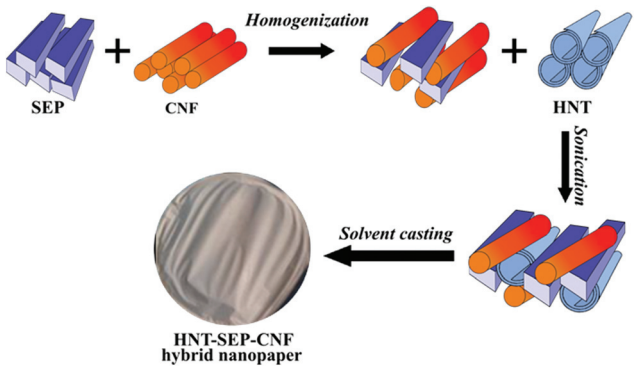

Fig. 1 Scheme of the procedures followed for the integration of HNT, SEP and CNF components leading to HNT–SEP–CNF hybrid nanopapers.

sition but also the combination of the components had a large influence on the film forming ability and therefore on their inherent properties. For instance, the HNT–SEP 1 : 1 (w/w) did not form a coherent film but rather an inconsistent, powdery material (Fig. 4b). Combining CNF with HNT rendered a self-supported film but with considerable defects (Fig. 4c). In contrast, the combination of SEP and CNF at a 1 : 1 ratio produced homogeneous films (Fig. 4d) in accordance with previous studies on CNF-sepiolite nanocomposites.[28] From these observations it can be concluded that the macroscopic aspect of the films largely depends on the CNF that plays a major role in providing consistency and mechanical integration to the nanopapers, while the presence of SEP produced an improved dispersion of the components as evident from Fig. 4a (HNT–SEP–CNF) and Fig. 4c (CNF–HNT). As indicated above, the increased sepiolite content (for instance 1 : 2 : 1, not shown) also results in non-uniform films undermining the film formation capacity of the CNF.

The microstructure of the films was further analyzed by X-ray diffraction (XRD) to corroborate possible intercalation within HNT silicate layers and preferential in-plane orientation of the fibers. The XRD pattern of the HNT–SEP–CNF hybrid nanopaper shows that the (001) reflection of halloysite at 12.0° 2θ is not displaced. This finding confirms that no intercalation occurred during the film formation (see Fig. S2† for the indexed pattern of pristine materials and the HNT–SEP–CNF hybrid nanopaper). The most prominent reflections of halloysite and sepiolite are present, whereas the low intensity reflections of the CNF are absent, which can be attributed to the relatively low crystallinity of the CNF. The intensity ratio of the 7.4° 2θ and 13.4° 2θ reflections in the patterns of sepiolite and of the HNT–SEP–CNF hybrid nanopaper (see Fig. S2†) changed from 15.9 to 2.4. It is well-known that a change in the relative intensity of peaks in a X-ray diffractogram of a given system is related to the precise orientation of the crystals and, in particular, in the present case the interactions between the CNF and sepiolite can lead to preferential orientations of the fibers.[28] Hence, this significant variation in the relative intensity of the (110) and (003) reflections suggests that the sepiolite fibers

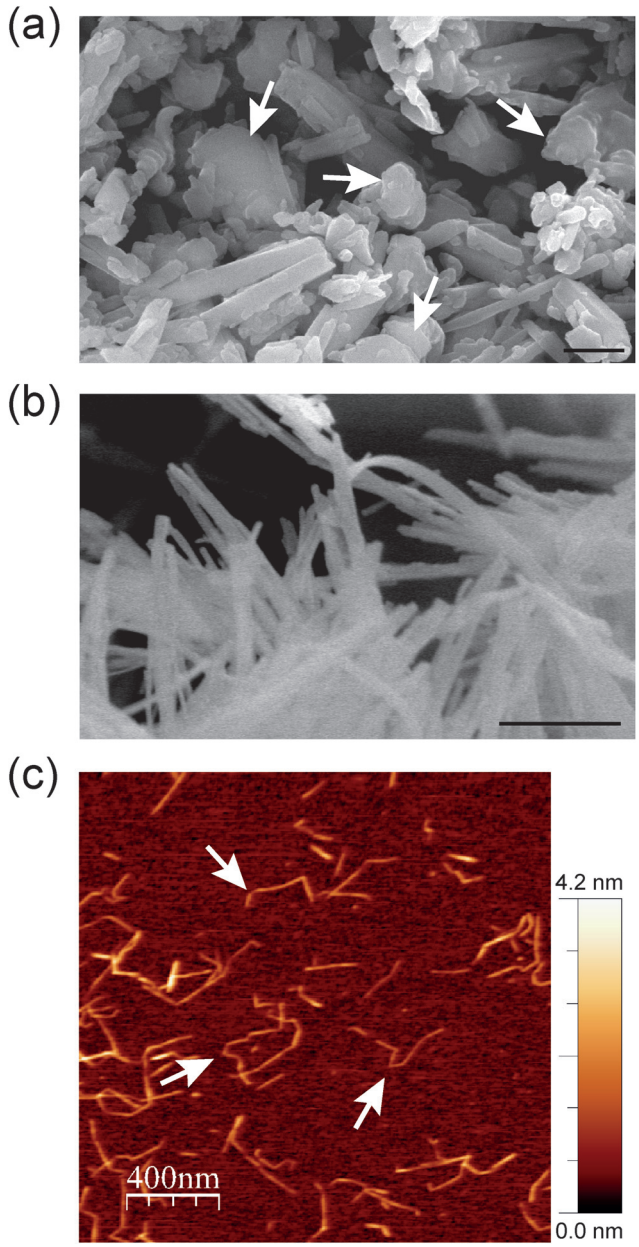

Fig. 2 SEM micrographs of (a) neat HNTs (white arrows represent the hexagonal kaolin sheets), (b) neat sepiolite and (c) the AFM image of the CNF (white arrows represent the fiber kinks). The scale bars in (a) and (b) refer to 500 nm.

have a preferred orientation within the hybrid nanopaper. Indeed, as the SEM images in Fig. 3 show, sepiolite seemed to be well accommodated within the plane of the film, and the fibers show an orientation that is probably induced by the interactions between the components.

The CNF-sepiolite interactions were investigated by IR spectroscopy to further elucidate their implication on the nematic ordering of the fibers. Fig. 5 shows the –OH stretching range (3730–3670 cm^{-1}) of the collected spectra of the individual pristine components and the HNT–SEP–CNF hybrid nanopaper, respectively. In particular, sepiolite has two bands at 3719

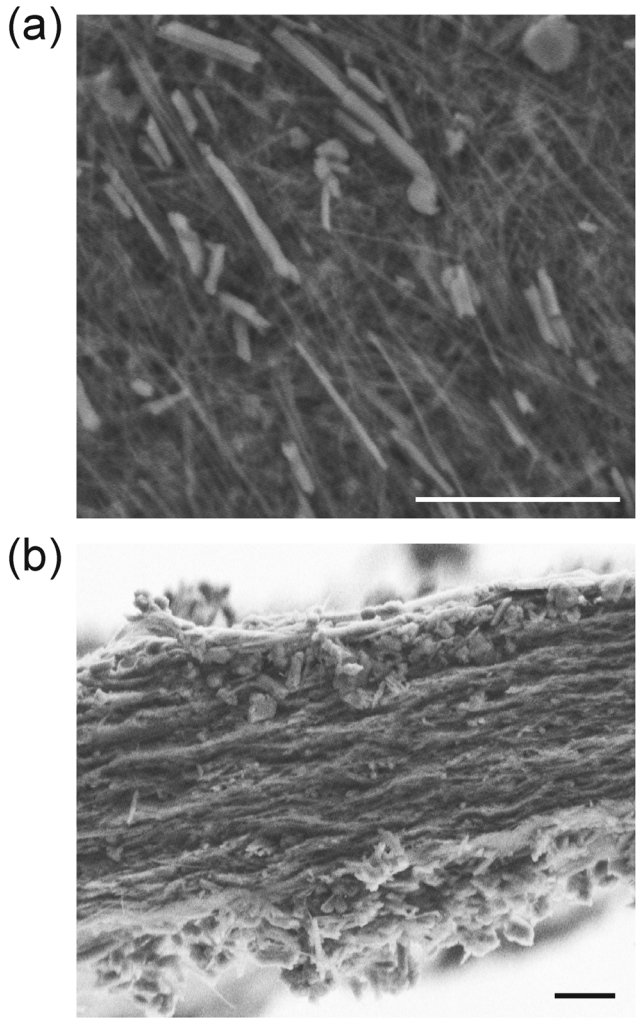

Fig. 3 SEM micrographs of (a) the surface and (b) the fracture cross-section of the 1 : 1 : 1 HNT–SEP–CNF hybrid nanopaper, respectively. The scale bars refer to 2 μm.

and 3680 cm^{-1} assigned to the –OH stretching vibrations of silanol groups and hydroxyl groups bonded to magnesium atoms, respectively.[31] The Mg–OH band at 3680 cm^{-1} remains practically unchanged in the spectrum of the hybrid HNT–SEP–CNF nanopaper as the hydroxyl groups bonded to magnesium atoms are not accessible. However, the band related to the silanol groups (3719 cm^{-1}) disappears, indicating the perturbation of these groups probably due to the hydrogen bonding interaction between Si–OH and the hydroxyl groups located on the surface of the CNF. In spite of this, certain interactions with the HNT clay may not be disregarded. Moreover, the two OH-stretching bands at 3695 and 3620 cm^{-1} related to the vibrations of the Al_2OH groups inside the lumen of halloysite[70] do not show relevant changes in the spectrum of the HNT–SEP–CNF hybrid nanopaper, suggesting the absence of interactions of the lumen with SEP and/or CNF. Thus, the H-bonding interactions between CNF and sepiolite that were conjectured to partake in the nematic ordering in the hybrid film are confirmed.

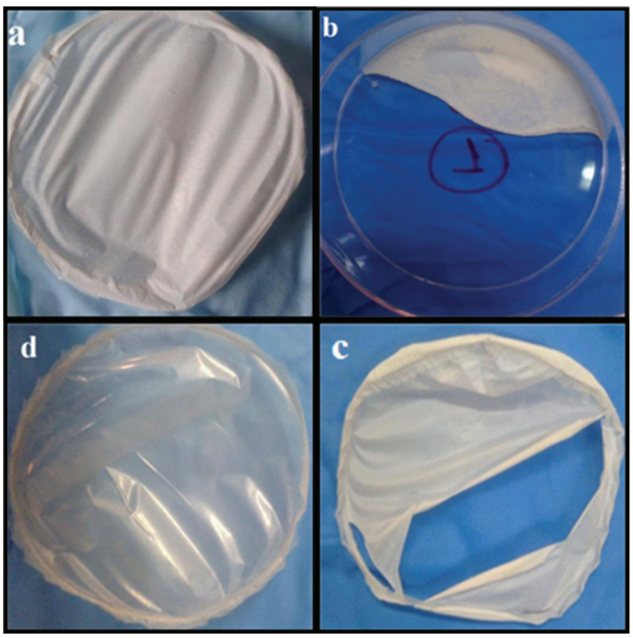

Fig. 4 Macroscopic aspect of various hybrid films prepared by combining HNT, SEP and CNF at different weight ratios: (a) 1 : 1 : 1 HNT–SEP–CNF nanopaper, (b) 1 : 1 HNT–SEP, (c) 1 : 1 HNT–CNF, and (d) 1 : 1 SEP–CNF.

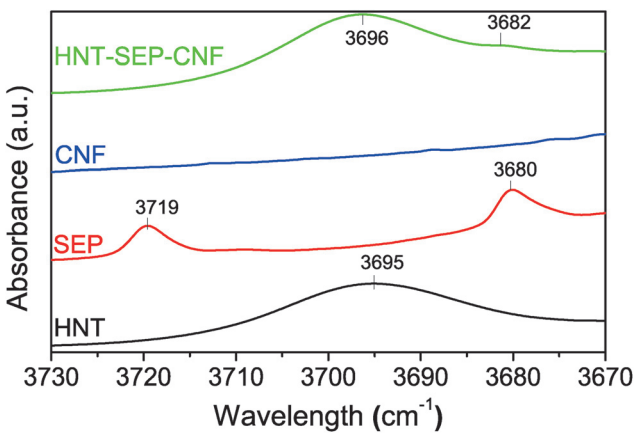

Fig. 5 FTIR spectra of the HNT, SEP, CNF and HNT–SEP–CNF hybrid nanopaper (3730–3670 cm^{-1} range). The complete spectra are provided in Fig. S3.†

The mechanical properties of the HNT–SEP–CNF hybrid nanopaper were evaluated from the stress–strain measurements to estimate the Young's modulus (Fig. S4†). It is noteworthy that the incorporation of sepiolite decreased the Young's modulus of the CNF nanopaper from 3.8 GPa to 1.8 GPa. However, the incorporation of HNTs into the SEP–CNF significantly enhanced the mechanical properties of the nanopaper with an increase to 3.2 GPa. These variations in the mechanical properties can be explained considering that halloysite can act as a reinforcement agent as observed elsewhere in cellulose films.[71]

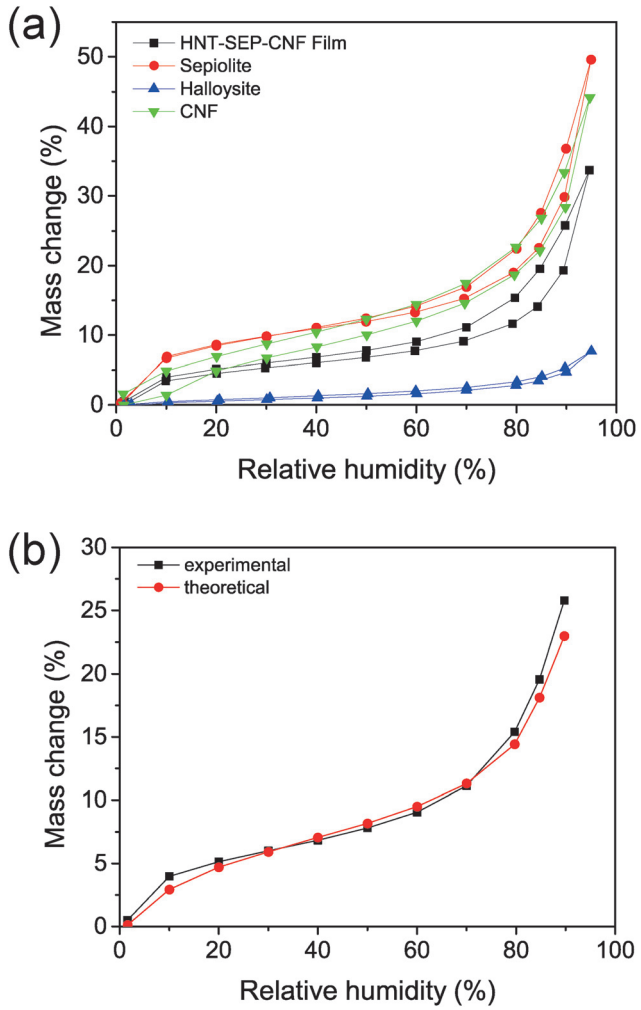

Fig. 6 Water sorption isotherms of (a) HNT (blue), sepiolite (red), CNF (green), and HNT–SEP–CNF (black) films. (b) Experimental *vs.* theoretical water sorption isotherms.

The wetting properties of the nanopapers were studied as they are relevant for topical drug delivery applications. Water sorption isotherms were recorded as shown in Fig. 6. The three individual components (*i.e.* SEP, CNF, and HNT) display different water sorption profiles (Fig. 6a). For instance, HNT adsorbs less water than sepiolite. Amongst other factors, this process is strongly influenced by both the specific surface area of the solids, *i.e.* 60 and 300 $m^2\ g^{-1}$ in the case of halloysite and sepiolite, respectively, and the presence of surface groups.[30,49] In particular, the external surface of HNT is constituted by hydrophobic Si–O–Si groups, whereas sepiolite displays hydrophilic Si–OH groups at the edges along the fiber length and the CNF presents a large number of –OH groups that are strongly hydrophilic. On the other hand, sepiolite and the CNF, the two fibrous components, show a similar mass change *vs.* relative humidity (% RH) value. Concerning the HNT–SEP–CNF hybrid nanopaper, the isotherm is between the isotherms of the HNT and SEP/CNF. A theoretical water adsorption isotherm was determined for the hybrid nanopaper by a simple numerical addition of the individual isotherms considering the 1 : 1 : 1 (w/w) ratio of HNT, SEP and CNF (Fig. 6b). This curve coincides with the experimental isotherm (Fig. 6a), which suggests that the wetting properties of the film are additive and not affected by the interactions between the individual components.

Table 1 Contact angle (θ_i), n and k_θ values of CNF, SEP–CNF and HNT–SEP–CNF films

	θ_i	n	$k_\theta\ (s^{-n})$
CNF	50 ± 1	0.48 ± 0.04	0.06 ± 0.01
SEP–CNF	31 ± 1	0.54 ± 0.09	0.03 ± 0.01
HNT–SEP–CNF	56 ± 5	0.27 ± 0.04	0.38 ± 0.09

The surface wetting properties of the different materials were also studied by water contact angle measurements on the films. The data were analyzed by fitting the contact angle θ *vs.* time τ curve with the following equation:

$$\Theta = \theta_i \exp(-k_\theta\ \tau^n) \quad (2)$$

where θ_i is the contact angle at $\tau = 0$, n represents the fractional values ascribable to the occurrence of absorption and spreading and k_θ is the rate of the former or the latter process.[71] The fitted data are reported in Table 1.

The contact angle value of the CNF nanopaper is 50°, whereas the value decreases to 31° in the case of CNF–SEP at a 1 : 1 weight ratio, confirming the strongly hydrophilic surface. It was also observed that the HNT–SEP–CNF 1 : 1 : 1 hybrid nanopaper displays a contact angle of 56°. This implies that the incorporation of halloysite notably decreases the wettability of HNT–SEP–CNF. The network of the self-assembled fibrils and nanotubes is also likely to display air-filled protrusions due to the increased surface roughness and thus giving rise to changes in the wettability of these materials. Indeed, similar observations were reported for polypropylene-HNT nanocomposites, in which the generation of a rough surface caused by the enrichment with HNT nanoparticles was ascribed to an improvement in the hydrophobic film properties.[72,73] Moreover, the data fitting of the Θ,τ curves revealed that both the spreading and absorption mechanisms of water took place for the studied nanopapers, that is $n = 0$ and 1 for pure absorption and pure spreading, respectively. For instance, the n value was ≈0.5 for the pure CNF and SEP–CNF films and it decreased to 0.27 for the HNT–SEP–CNF nanopaper, reflecting a major role in the absorption mechanism of water into the material.

3.2. Uptake of salicylic acid and ibuprofen by HNT–SEP–CNF hybrid nanopapers

As mentioned above, the HNT–SEP–CNF hybrid nanopapers were evaluated as drug delivery systems (DDS) using two model drugs, SA and IBU, due to their widespread use in topical applications including injury cure. The SA loading into HNT was 8.4 wt% as deduced from the elemental analysis, which shows a similar value as reported for other halloysite-SA

systems.[74] The total amount of IBU loaded into HNT was 5.1 wt%. It is interesting to note that the SA loading at pH 8 to maximize the negative charge of the drug allowed a larger amount of SA to be adsorbed on HNT as compared with IBU loading values.

The FTIR spectra of SA, HNT and HNT–SA were collected to investigate the possible interactions of SA with HNT (Fig. S5a†). These data indicate that the interaction with HNT changes the π-electron density of the benzene ring of the salicylate, as inferred from the shift of the absorption bands of the C=C vibrations from 1597, 1485 and 1468 cm^{-1} to 1606, 1473 and 1463 cm^{-1}, respectively. In addition, it was found that the ν_{as} vibration of $-COO^-$ was shifted from 1582 to 1577 cm^{-1}, meanwhile the band at 1377 cm^{-1} of the ν_s vibration of $-COO^-$ splits into two components, *i.e.* 1387 and 1375 cm^{-1}.[74] Moreover, the stretching and bending vibrations of Ph–OH at 1248 cm^{-1} and 1319 cm^{-1} respectively, shift, which suggests that the phenolic group is involved in the interaction between the salicylate and AlOH groups inside the HNT lumen. For what concerns the IBU-loaded HNTs, the FTIR spectra (Fig. S5b and c†) show the appearance of the characteristic bands at 2956, 2925, 2869, 2849 and 1550 cm^{-1} of IBU.[75] This is attributed to the successful entrapment of IBU in the lumen of the nanotube.

The N_2 adsorption/desorption isotherms for pristine HNT, salicylate loaded HNT and ibuprofen loaded HNT (Fig. S6†) were collected in order to verify the entrapment of the molecules in the HNT lumen. After loading, the type IV isotherm persisted but an appreciable reduction in the BET surface area, pore surface area, and pore volume in comparison with pristine HNT was observed (Table 2).

After SA loading into HNT, the BET surface area dropped from 27.3 to 20.2 $m^2\ g^{-1}$, the mesopore area decreased from 23.2 to 17.8 $m^2\ g^{-1}$ and the mesopore volume was reduced from 0.062 to 0.054 $cm^3\ g^{-1}$. This suggests that the SA inside the halloysite lumen produced a partial pore blockage accounting for the BET surface area reduction and the corresponding reduction in the mesopore area and volume parameters. The modification of these parameters is more noticeable for HNT–SA than HNT–IBU reflecting the higher SA uptake.

The release profiles for SA and IBU from the HNT and HNT–SEP–CNF nanopapers were collected to determine the release kinetics (Fig. 7).

The profiles show that more than 90% of salicylic acid was released from HNT within 60 min while less than 80% was released from the HNT–SEP–CNF hybrid nanopaper during the same period of time. Moreover, ibuprofen is released from

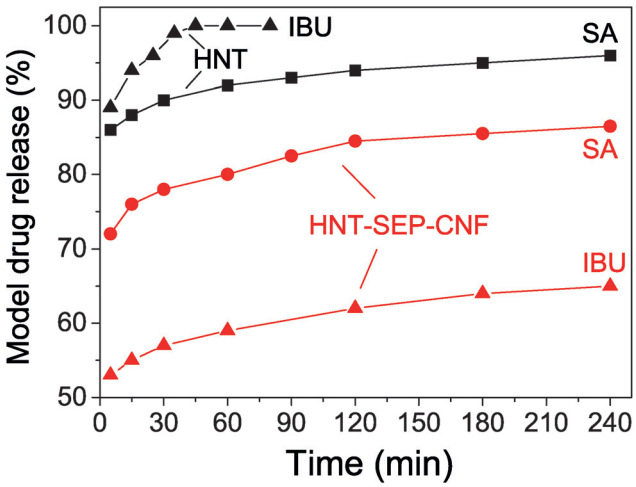

Fig. 7 Release profiles of salicylic acid (SA) and ibuprofen (IBU) from the loaded HNTs and loaded HNT–SEP–CNF hybrid nanopaper.

HNT at an even higher rate, while the release rate from the HNT–SEP–CNF film was considerably lower. Almost 60% of ibuprofen was released from the film within 60 min *vs.* 100% release from HNT. After 4 hours, only *ca.* 65% of IBU was released. These observations could be explained by invoking the very high solubility of the drugs (salicylate and ibuprofen sodium salts) in water. The solubility of IBU in water is 100 mg mL^{-1} while for SA it is 50 mg mL^{-1}. This may explain why IBU is released faster from HNT than SA. In contrast, in the HNT–SEP–CNF hybrid nanopaper, the release rate of the drug is lower possibly due to the multiple interactions with the halloysite, sepiolite and cellulose nanofibers. In this case, once the drugs are released from the lumen, the interactions with the other matrix components are important and determine the release kinetics. For instance, strong interactions have been reported to exist between IBU and the nanocellulose,[76] which could explain the slower IBU release kinetics from the HNT–SEP–CNF hybrid nanopaper as compared to SA. In addition, the openings of the nanotubes could be partially obstructed by the particular texture of the film and thus, sustained the drug release. Moreover, the particular diffusion mechanism of the drugs inside the nanotube lumen and through the nanocomposite matrix plays an important role. For instance, the particular position of the loaded drug inside the nanotubes, at the edges or at the center of the lumen, has been reported to deeply affect the release kinetics due to the diffusion path of the guest molecules which is faster in the first case and slower in the second case.[70]

Table 2 The BET surface area, pore surface area, S_{mes}, and pore volume, V_{mes}, of pristine HNT, SA loaded HNT and IBU loaded HNT

	S_{BET} ($m^2\ g^{-1}$)	S_{mes} ($m^2\ g^{-1}$)	V_{mes} ($cm^3\ g^{-1}$)
HNTs	27.3	23.2	0.062
HNT + SA	20.2	17.8	0.054
HNT + IBU	24.6	21.9	0.057

3.3. *In vitro* antibacterial assay

Based on the sustained SA release from the HNT–SEP–CNF hybrid nanopapers, the studies of antibacterial activity were performed to evaluate this new type of delivery system for topical applications. Therefore, the studies were carried out against the typically used Gram-negative *E. coli* and Gram-positive *S. aureus* bacteria under neutral and acidic (pH = 5.5) con-

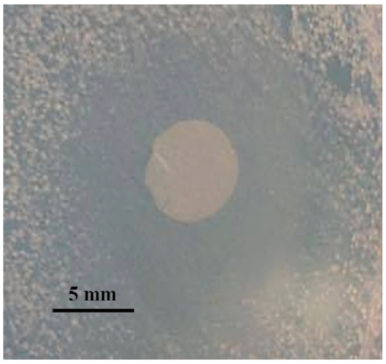

Fig. 8 Inhibition zone of the salicylic acid loaded HNT–SEP–CNF hybrid nanopaper against Gram-positive *S. aureus* at pH = 5.5.

ditions by means of the disk diffusion method.[52] The positive controls for salicylate are displayed in Fig. S6.†

It was observed that the SA loaded in HNT and then incorporated to the HNT–SEP–CNF nanopaper displays antimicrobial activity and shows an effect when it is used against *S. aureus* at pH = 5.5, as confirmed by the positive controls (Fig. S7d†).

The result of the trials is shown in Fig. 8, where the formation of the inhibition zone is clearly observable. Moreover, its average diameter is in the same order of magnitude of salicylic acid loaded pectin-HNT bionanocomposites[70] thus, confirming the activity of the drug loaded HNT–SEP–CNF hybrid nanopaper.

4. Conclusions

A new type of biohybrid material processed as a film was prepared by co-assembling nanotubular halloysite, fibrous sepiolite, and cellulose nanofibers. The 1 : 1 : 1 (w/w) ratio of the three components was found to render homogeneous and self-supported films displaying reasonable mechanical properties and endorsing suitable characteristics for the proposed applications. Different characterization techniques confirm the short-range interactions between the organic and the inorganic components, mainly occurring through hydrogen bonding between the hydroxyl groups.

The incorporation of HNT allows controlling the textural and surface chemistry characteristics of the resulting film including its mechanical properties and the wetting behavior. For instance, we observed an increased Young's modulus value and a less hydrophilic surface for the HNT–SEP–CNF hybrid nanopaper compared to the SEP–CNF films. The interaction of HNT, SEP, and CNF renders multifunctional hybrid nanopapers that can be deployed for further functionalization in a wide range of applications. In this way, they were evaluated as drug delivery systems using salicylic acid and ibuprofen due to their conventional use in topical treatments. The results proved the effective encapsulation of the drugs into the positively charged HNT lumen and more sustained release kinetics for the hybrid nanopaper as compared to the loaded neat halloysite. Furthermore, the evaluation of the antimicrobial activity studies against Gram-positive and Gram-negative bacteria proved the effective inhibition of *S. aureus* growth at pH = 5.5 confirming the interest of this new type of biohybrid material in controlled delivery applications. Besides, these nanopapers also offer interesting possibilities for further applications in view of the different chemical features and functional groups of the components.

Conflicts of interest

The authors declare no conflict of interest.

Acknowledgements

The authors thank the MINECO (Spain) and FEDER (EU) for financial support (project MAT2015-71117-R). LL and GDL acknowledge the University of Palermo for the "UOB21 Borse di studio finalizzate alla ricerca" grants. BW thanks the MINECO for the IJCI contract (IJCI-2015-23886). The authors also thank Ms Paloma Encinas from INIA and M. Mar Blanco-Gutierrez from the Veterinary Faculty of the Complutense University of Madrid for providing bacterial strains.

References

1 E. Ruiz-Hitzky, P. Aranda, M. Darder and G. Rytwo, *J. Mater. Chem.*, 2010, **20**, 9306–9321.
2 E. Ruiz-Hitzky, M. Darder, F. M. Fernandes, B. Wicklein, A. C. S. Alcântara and P. Aranda, *Prog. Polym. Sci.*, 2013, **38**, 1392–1414.
3 T. Hueckel and S. Sacanna, *ACS Nano*, 2018, **12**, 3533–3540.
4 E. Abdullayev and Y. Lvov, *J. Mater. Chem. B*, 2013, **1**, 2894–2903.
5 M. Catauro, E. Tranquillo, F. Barrino, I. Blanco, F. Dal Poggetto and D. Naviglio, *Materials*, 2018, **11**, 2270.
6 M. Faustini, L. Nicole, E. Ruiz-Hitzky and C. Sanchez, *Adv. Funct. Mater.*, 2018, **28**, 1704158.
7 E. Paineau, M.-E. M. Krapf, M.-S. Amara, N. V. Matskova, I. Dozov, S. Rouzière, A. Thill, P. Launois and P. Davidson, *Nat. Commun.*, 2016, **7**, 10271.
8 L. Lisuzzo, G. Cavallaro, S. Milioto and G. Lazzara, *New J. Chem.*, 2019, **43**, 10887–10893.
9 E. P. Rebitski, P. Aranda, M. Darder, R. Carraro and E. Ruiz-Hitzky, *Dalton Trans.*, 2018, **47**, 3185–3192.
10 E. P. Rebitski, G. P. Souza, S. A. A. Santana, S. B. C. Pergher and A. C. S. Alcântara, *Appl. Clay Sci.*, 2019, **173**, 35–45.
11 M. Djellali, P. Aranda and E. Ruiz-Hitzky, *Appl. Clay Sci.*, 2019, **171**, 65–73.
12 B. Huang, M. Liu and C. Zhou, *Carbohydr. Polym.*, 2017, **175**, 689–698.
13 G. Gorrasi, R. Pantani, M. Murariu and P. Dubois, *Macromol. Mater. Eng.*, 2014, **299**, 104–115.

14 Y. Fukushima and S. Inagaki, *J. Inclusion Phenom.*, 1987, **5**, 473–482.
15 F. Li, E. Mascheroni and L. Piergiovanni, *Packag. Technol. Sci.*, 2015, **28**, 475–508.
16 H. Zhu, Z. Fang, C. Preston, Y. Li and L. Hu, *Energy Environ. Sci.*, 2014, **7**, 269–287.
17 B. Wicklein, A. Kocjan, G. Salazar-Alvarez, F. Carosio, G. Camino, M. Antonietti and L. Bergström, *Nat. Nanotechnol.*, 2015, **10**, 277–283.
18 Y. Xue, Z. Mou and H. Xiao, *Nanoscale*, 2017, **9**, 14758–14781.
19 L. Shun and H. Jianguo, *Adv. Mater.*, 2016, **28**, 1143–1158.
20 B. Wicklein, D. Kocjan, F. Carosio, G. Camino and L. Bergström, *Chem. Mater.*, 2016, **28**, 1985–1989.
21 M. Pääkkö, M. Ankerfors, H. Kosonen, A. Nykänen, S. Ahola, M. Österberg, J. Ruokolainen, J. Laine, P. T. Larsson, O. Ikkala and T. Lindström, *Biomacromolecules*, 2007, **8**, 1934–1941.
22 T. Saito, S. Kimura, Y. Nishiyama and A. Isogai, *Biomacromolecules*, 2007, **8**, 2485–2491.
23 R. J. Moon, A. Martini, J. Nairn, J. Simonsen and J. Youngblood, *Chem. Soc. Rev.*, 2011, **40**, 3941–3994.
24 A. Hajian, S. B. Lindström, T. Pettersson, M. M. Hamedi and L. Wågberg, *Nano Lett.*, 2017, **17**, 1439–1447.
25 B. Wicklein, A. M. Diem, A. Knöller, M. S. Cavalcante, L. Bergström, J. Bill and Z. Burghard, *Adv. Funct. Mater.*, 2017, 1704274.
26 C. Aulin, G. Salazar-Alvarez and T. Lindstrom, *Nanoscale*, 2012, **4**, 6622–6628.
27 K. Yao, S. Huang, H. Tang, Y. Xu, G. Buntkowsky, L. A. Berglund and Q. Zhou, *ACS Appl. Mater. Interfaces*, 2017, **9**, 20169–20178.
28 M. M. Gonzalez del Campo, M. Darder, P. Aranda, M. Akkari, Y. Huttel, A. Mayoral, J. Bettini and E. Ruiz-Hitzky, *Adv. Funct. Mater.*, 2017, 1703048.
29 M. Ghanadpour, B. Wicklein, F. Carosio and L. Wagberg, *Nanoscale*, 2018, **10**, 4085–4095.
30 E. Ruiz-Hitzky, *J. Mater. Chem.*, 2001, **11**, 86–91.
31 M. Akkari, P. Aranda, A. Mayoral, M. García-Hernández, A. B. H. Amara and E. Ruiz-Hitzky, *J. Hazard. Mater.*, 2017, **340**, 281–290.
32 J. L. Ahlrichs, C. Serna and J. M. Serratosa, *Clays Clay Miner.*, 1975, **23**, 119–124.
33 F. M. Fernandes and E. Ruiz-Hitzky, *Carbon*, 2014, **72**, 296–303.
34 E. Ruiz-Hitzky, M. M. C. Sobral, A. Gómez-Avilés, C. Nunes, C. Ruiz-García, P. Ferreira and P. Aranda, *Adv. Funct. Mater.*, 2016, **26**, 7394–7405.
35 P. Aranda and E. Ruiz-Hitzky, *Chem. Rec.*, 2018, **18**, 1125–1137.
36 P. Pasbakhsh, G. J. Churchman and J. L. Keeling, *Appl. Clay Sci.*, 2013, **74**, 47–57.
37 Y. Lvov and E. Abdullayev, *Prog. Polym. Sci.*, 2013, **38**, 1690–1719.
38 A. Takahara and Y. Higaki, *RSC Smart Mater.*, 2017, 131–156.
39 E. Abdullayev, A. Joshi, W. Wei, Y. Zhao and Y. Lvov, *ACS Nano*, 2012, **6**, 7216–7226.
40 M. R. Dzamukova, E. A. Naumenko, Y. M. Lvov and R. F. Fakhrullin, *Sci. Rep.*, 2015, **5**, 10560.
41 L. Lisuzzo, G. Cavallaro, F. Parisi, S. Milioto and G. Lazzara, *Ceram. Int.*, 2019, **45**, 2858–2865.
42 G. Cavallaro, G. Lazzara, S. Milioto, F. Parisi and V. Sanzillo, *ACS Appl. Mater. Interfaces*, 2014, **6**, 606–612.
43 J. Tully, R. Yendluri and Y. Lvov, *Biomacromolecules*, 2016, **17**, 615–621.
44 H. Zhang, C. Cheng, H. Song, L. Bai, Y. Cheng, X. Ba and Y. Wu, *Chem. Commun.*, 2019, **55**, 1040–1043.
45 G. Cavallaro, I. Grillo, M. Gradzielski and G. Lazzara, *J. Phys. Chem. C*, 2016, **120**, 13492–13502.
46 G. Cavallaro, G. Lazzara, L. Lisuzzo, S. Milioto and F. Parisi, *Nanotechnology*, 2018, **29**, 325702.
47 F. Liu, L. Bai, H. Zhang, H. Song, L. Hu, Y. Wu and X. Ba, *ACS Appl. Mater. Interfaces*, 2017, **9**, 31626–31633.
48 B. Huang, M. Liu and C. Zhou, *Cellulose*, 2017, **24**, 2861–2875.
49 M. Du, B. Guo and D. Jia, *Polym. Int.*, 2010, **59**, 574–582.
50 G. Lazzara, G. Cavallaro, A. Panchal, R. Fakhrullin, A. Stavitskaya, V. Vinokurov and Y. Lvov, *Curr. Opin. Colloid Interface Sci.*, 2018, **35**, 42–50.
51 G. Cavallaro, G. Lazzara, S. Milioto, F. Parisi, V. Evtugyn, E. Rozhina and R. Fakhrullin, *ACS Appl. Mater. Interfaces*, 2018, **10**, 8265–8273.
52 G. Cavallaro, S. Milioto, F. Parisi and G. Lazzara, *ACS Appl. Mater. Interfaces*, 2018, **10**, 27355–27364.
53 H. Wan, H. Xiong, X. Liu, G. Chen, N. Zhang, H. Wang, R. Ma and G. Qiu, *Dalton Trans.*, 2018, **47**, 7522–7527.
54 M. M. Najafpour and E. Amini, *Dalton Trans.*, 2015, **44**, 15441–15449.
55 S. Sadjadi, M. Akbari, E. Monflier, M. M. Heravi and B. Leger, *New J. Chem.*, 2018, **42**, 15733–15742.
56 G. I. Fakhrullina, F. S. Akhatova, Y. M. Lvov and R. F. Fakhrullin, *Environ. Sci.: Nano*, 2015, **2**, 54–59.
57 G. Cavallaro, G. Lazzara and S. Milioto, *J. Phys. Chem. C*, 2012, **116**, 21932–21938.
58 G. Lo Dico, B. Wicklein, L. Lisuzzo, G. Lazzara, P. Aranda and E. Ruiz-Hitzky, *Beilstein J. Nanotechnol.*, 2019, **10**, 1303–1315.
59 R. Zurita, J. Puiggalí and A. Rodríguez-Galán, *Macromol. Biosci.*, 2006, **6**, 767–775.
60 R. Abdeen and N. Salahuddin, *Eur. J. Chem.*, 2013, 1–9.
61 M. Haraketi, K. Hosni and E. Srasra, *Surf. Eng. Appl. Electrochem.*, 2017, **53**, 360–370.
62 Ú. Fillat, B. Wicklein, R. Martín-Sampedro, D. Ibarra, E. Ruiz-Hitzky, C. Valencia, A. Sarrión, E. Castro and M. E. Eugenio, *Carbohydr. Polym.*, 2018, **179**, 252–261.
63 L. Ji, W. Qiao, Y. Zhang, H. Wu, S. Miao, Z. Cheng, Q. Gong, J. Liang and A. Zhu, *Mater. Sci. Eng., C*, 2017, **78**, 362–369.
64 L. Lisuzzo, G. Cavallaro, P. Pasbakhsh, S. Milioto and G. Lazzara, *J. Colloid Interface Sci.*, 2019, **547**, 361–369.

65 D. Yu, J. Wang, W. Hu and R. Guo, *Mater. Des.*, 2017, **129**, 103–110.
66 W. Yang, Z. Zhao, K. Wu, R. Huang, T. Liu, H. Jiang, F. Chen and Q. Fu, *J. Mater. Chem. C*, 2017, **5**, 3748–3756.
67 M. Zhao, F. Ansari, M. Takeuchi, M. Shimizu, T. Saito, L. A. Berglund and A. Isogai, *Nanoscale Horiz.*, 2018, **3**, 28–34.
68 A. N. Fernandes, L. H. Thomas, C. M. Altaner, P. Callow, V. T. Forsyth, D. C. Apperley, C. J. Kennedy and M. C. Jarvis, *Proc. Natl. Acad. Sci. U. S. A.*, 2011, **108**, E1195–E1203.
69 R. Shinoda, T. Saito, Y. Okita and A. Isogai, *Biomacromolecules*, 2012, **13**, 842–849.
70 M. Makaremi, P. Pasbakhsh, G. Cavallaro, G. Lazzara, Y. K. Aw, S. M. Lee and S. Milioto, *ACS Appl. Mater. Interfaces*, 2017, **9**, 17476–17488.
71 G. Cavallaro, D. I. Donato, G. Lazzara and S. Milioto, *J. Phys. Chem. C*, 2011, **115**, 20491–20498.
72 Q. Zhou, K. P. Pramoda, J.-M. Lee, K. Wang and L. S. Loo, *J. Colloid Interface Sci.*, 2011, **355**, 222–230.
73 A. Marmur, *Langmuir*, 2008, **24**, 7573–7579.
74 A. Spepi, C. Duce, A. Pedone, D. Presti, J.-G. Rivera, V. Ierardi and M. R. Tiné, *J. Phys. Chem. C*, 2016, **120**, 26759–26769.
75 H. Li, X. Zhu, H. Zhou and S. Zhong, *Colloids Surf., A*, 2015, **487**, 154–161.
76 G. Chantereau, M. Sharma, A. Abednejad, B. M. Neves, G. Sèbe, V. Coma, M. G. Freire, C. S. R. Freire and A. J. D. Silvestre, *ACS Sustainable Chem. Eng.*, 2019, **7**, 14126–14134.